Available online at www.sciencedirect.com
ScienceDirect
Nuclear Instruments and Methods in Physics Research B 266 (2008) 3467–3480
NIM B
Beam Interactions with Materials & Atoms
www.elsevier.com/locate/nimb

MOCADI_FUSION: Extension of the Monte-Carlo code MOCADI to heavy-ion fusion–evaporation reactions

M. Mazzocco [a,*,1], D. Ackermann [a], M. Block [a], H. Geissel [a,b], F. Herfurth [a], F.P. Heßberger [a], S. Hofmann [a,c], N. Iwasa [d], K. Nishio [a,e], W.R. Plaß [b], C. Scheidenberger [a,b], H. Weick [a], M. Winkler [a], The SHIPTRAP Collaboration

[a] *Gesellschaft für Schwerionenforschung (GSI), Planckstrasse 1, D-64291 Darmstadt, Germany*
[b] *Justus Liebig-Universität Gießen, II. Physikalisches Institut, Heinrich-Buff-Ring 16, D-35390 Gießen, Germany*
[c] *Johann Wolfgang Goethe-Universität Frankfurt, Institut für Kernphysik, D-60054 Frankfurt am Main, Germany*
[d] *Department of Physics, Tohoku University, Sendai, Miyagi 980-8578, Japan*
[e] *Japanese Atomic Energy Agency (JAEA), Tokai, Ibaraki 319-1195, Japan*

Received 11 February 2008; received in revised form 24 April 2008
Available online 7 May 2008

Abstract

We have recently developed a code, called MOCADI_FUSION, for tracing fusion–evaporation residues (ERs) through matter within ion-optical systems. The program is based on the existing Monte-Carlo code MOCADI, which has been extended by including the kinematics of fusion–evaporation reactions and the atomic interaction of the ERs with the target atoms. The ion optics of the experimental set-up used for the selection of the desired species is combined with the phase-space distribution of the ERs at the target exit into MOCADI to evaluate the secondary beam properties (beam profile, separation quality, transmission, etc.) along the separator. The code has been tested for the velocity filter SHIP at GSI, and it reproduces the set-up characteristics (angular, charge state and velocity acceptances) and the experimental transmission data. MOCADI_FUSION has been also used for the SHIPTRAP experiment to evaluate the range distribution of the ERs in the gas cell and to estimate the overall SHIPTRAP efficiency.

PACS: 24.10.Lx; 24.60.Dr; 25.60.Pj

Keywords: Monte-Carlo simulations; Fusion–evaporation reactions; Statistical model

1. Introduction

Experiments aimed at studying the properties of exotic nuclei far from stability often have to deal with very small production cross sections. Very low particle yields require: (i) the development of ion sources and accelerators able to provide high primary beam currents; (ii) the design of target systems adapted to withstand very large energy deposits; (iii) the detailed knowledge of the reaction kinematics occurring inside the production target; (iv) the design of highly selective beam separators to suppress the huge background due to scattered particles from the high intensity primary beam and unwanted species; (v) the elaboration of high-efficiency detection set-ups able to give prominence to the peculiar features of the nuclei under analysis. Within this framework, simulations are of crucial importance for the development and the optimization of all the devices involved in such complex experiments.

The Monte-Carlo transport code MOCADI [1] has already proved to be an appropriate tool to accomplish some of these tasks. It was extensively used for the design

* Corresponding author.
E-mail address: marco.mazzocco@pd.infn.it (M. Mazzocco).
[1] Present address: Dipartimento di Fisica and INFN – Sezione di Padova, via Marzolo 8, I-35131 Padova, Italy.

0168-583X/$ - see front matter © 2008 Elsevier B.V. All rights reserved.
doi:10.1016/j.nimb.2008.04.017

of the GSI Fragment Separator (FRS) [2] and for the coupling of the Experimental Storage Ring (ESR) [3] with the FRS. Presently it is being employed for the study of the Super-FRS [4] within the FAIR project [5]. This program also has been a very useful support for the preparation and the analysis of several experiments involving secondary beam production via high-energy fragmentation and fission reactions.

The development of MOCADI was started in the late eighties at GSI (Darmstadt, Germany) with the purpose of producing a universal tool for tracing an ensemble of relativistic ions through matter within ion-optical systems, taking into account atomic and nuclear interaction and high-order image aberrations. We have recently extended MOCADI to low-energy reactions in order to make it also applicable to fusion–evaporation processes. Heavy-ion fusion reactions are typically employed for the synthesis of super-heavy elements ($Z \geqslant 100$) [6], since their short half-lives do not permit their access via *n*-capture followed by β^--decay. In addition, exotic nuclei in the neutron deficient region around ^{100}Sn are easily accessible via fusion reactions. This region is rather interesting, since it corresponds to the heaviest simultaneous closure of shells for equal proton and neutron numbers ($N = Z = 50$). This feature leads to a large variety of phenomena: proton [7] and α [8] radioactivity above ^{100}Sn, 2-proton radioactivity from the (21^+) isomeric state in ^{94}Ag [9], emission of intermediate mass fragments (IMFs, $Z > 2$) [10] and the fast $\pi g_{9/2} \rightarrow \nu g_{7/2}$ Gamow–Teller transition [11]. Moreover, ^{107}Te is expected to be the end-point of the astrophysical *rp*-process [12] and all lighter nuclei close to the proton drip line are deeply involved in this stellar process.

Since the cross sections for the production of such exotic and super-heavy nuclei are in the μb–nb and pb–fb region, respectively, a precise knowledge of reaction kinematics, beam transport and focusing, as well as nuclear and atomic interaction with matter, is needed to select the desired evaporation residues (ERs) and to provide an efficient background suppression. Up to now LisFus [13], within the package LISE [14], has been the only computer code available on the market able to provide a comprehensive description of all the physical ingredients involved in the production and separation of ERs. This program has been developed mainly for fast calculations and uses macroscopic analytical approaches to model the fusion–evaporation cascades and to determine the transport through the separator. In our case, we have opted for a fully Monte-Carlo treatment of the ERs, from their production inside the reaction target to their detection at the end of the spectrometer. Of course this is at the cost of a much longer CPU time, but our results are more accurate since no algebraic assumptions are made on the velocity and angular distributions of the produced particles, the ion optics is more flexible and calculated to an higher order and the ion-optical elements are included in the calculations with their real apertures. As a first application, we used our extended version of MOCADI, called MOCADI_FUSION, for the velocity filter SHIP [15] coupled to the double Penning trap system SHIPTRAP [16] in order to simulate the production, separation and stopping of medium-heavy fusion products.

The paper is organized as follows: Section 2 will contain a detailed description of the updated MOCADI version and will present the ion-optical calculations for the separator SHIP. Section 3 will describe some applications related to the extension of the code, in particular with respect to the comparison with presently available tabulated or experimental data. Some concluding remarks will be drawn in Section 4.

2. Description of the code MOCADI_FUSION

The Monte-Carlo transport code MOCADI has been already described in detail in [1], therefore in this paper we will briefly summarize its main characteristics and we will mainly concentrate on the new features.

MOCADI is written using the programming language C and it has a modular structure. Each module represents a unit located along the beam-line. These units can consist of:

- optical elements, such as dipole magnets, quadrupoles, hexapoles, electric sectors;
- geometrical constraints, such as drift lengths, collimators, slits;
- matter, i.e. targets, degrader foils, gas volumes, where particles can undergo atomic or nuclear interaction.

The modules receive appropriate input parameters such as field strength, energy, and have to be placed in sequence to reproduce the experimental layout. The code then traces an ensemble of particles through the whole ion-optical system. The modularity of the code makes it very flexible and applicable to nearly all experimental set-ups.

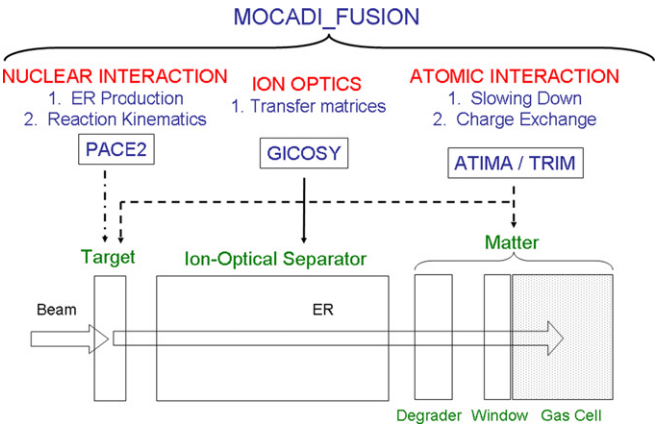

Fig. 1. Schematic view of the MOCADI_FUSION code structure and its relation to the experimental set-up, here SHIP [15] and SHIPTRAP [16]. "Slowing down" includes energy, angular and range distributions, while the charge state distribution is described by its mean value and variance.

MOCADI_FUSION has been developed within the framework of MOCADI and its structure is illustrated schematically in Fig. 1. Since in the following we will mainly exploit the code at the SHIP and SHIPTRAP facilities, Fig. 1 shows some specific connections to these equipments.

The key ingredients of MOCADI_FUSION are: (i) the description of the nuclear interaction generating the ERs (see Section 2.1); (ii) the treatment of the atomic interaction of the ERs (see Section 2.2); (iii) the calculation of the separator ion optics (see Section 2.3). We used the statistical code PACE2 [17] to describe the nuclear reaction process leading to the production of the ERs, while the atomic interaction of the ERs with the target atoms can be treated either with ATIMA [18] or TRIM [19]. This procedure allows to define the phase-space of the ERs at the target exit via an event-by-event Monte-Carlo calculation. At the same time the ion optics of the separator used for the selection of the desired nuclear species is calculated with the code GICOSY [20], which computes the transfer matrices of all the ion optical elements. These matrices are afterwords combined together with the phase-space of the ERs and with an accurate geometrical description of the experimental lay-out into a MOCADI input file. This transport code finally traces the particle trajectories through the separator and calculates the secondary beam properties, i.e. beam profile, separation quality, transmission, at different stages along the set-up (see Section 2.4 for a detailed example of ERs traced along the velocity filter SHIP).

2.1. Nuclear interaction

Fusion–evaporation processes are included in MOCADI_FUSION in terms of cross sections and reaction kinematics using the code PACE2, which is based on the statistical model.

The projectiles impinge on the target with the beam energy E_0, as provided by the accelerator. The nuclear interaction (fusion process) is supposed to occur at a random depth within the target thickness. For all the events the same interaction energy $E_{\text{int}} = E_0 - \Delta E/2$ is assumed, with ΔE the total energy loss of the projectile through the whole target. This approximation has proved to be a valid assumption for moderate energy losses ($\Delta E \leqslant$ 5–10 MeV), thin targets ($\leqslant 0.5$ mg/cm^2) and interaction energies above the Coulomb barrier. We tested this hypothesis for the reaction ^{50}Ti (215 MeV) + ^{120}Sn (0.5 mg/cm^2) → ^{166}Hf + 4n. We divided the whole target thickness into ten 50-μg/cm^2 thick bins and we applied MOCADI_FUSION to each slice. We computed the primary beam energy after each interval and we used these values as interaction energies for fusion–evaporation reactions at different depths within the target. The comparison between the predictions given by the two approaches for the mean kinetic energy of the ERs (see Fig. 2(a)) and for their angular divergence at the target exit showed an agreement within 1.5–2%. Simulations carried out for thicker target thicknesses and displayed in Fig. 2 show that the assumption of a fixed interaction energy for all fusion events is an overall good approximation to evaluate the mean kinetic energy of the ERs, while the width of the energy spectrum is usually overpredicted. The overestimation is about 2% for a target thickness of 0.5 mg/cm^2 and increases up to 8–9% and 11–12% at 1.0 mg/cm^2 (see Fig. 2(b)) and 1.5 mg/cm^2 (see Fig. 2(c)), respectively. Thus we can conclude that for moderate target thicknesses the kinematics of the ERs are only slightly affected by the assumption of a fixed interaction energy. Of course, in case of heavy projectiles impinging on thicker targets and for the production of super-heavy nuclei, the actual dependence of the fusion excitation function on the interaction energy should be properly included in the calculations.

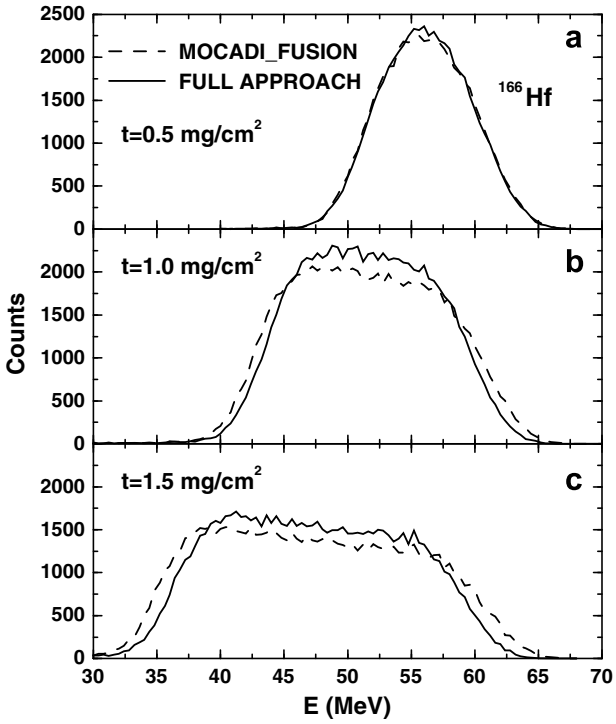

Fig. 2. Calculated energy spectra at the target exit for ^{166}Hf ERs produced in the fusion reaction ^{50}Ti + ^{120}Sn. Panels (a–c) refer to a target thickness of 0.5, 1.0 and 1.5 mg/cm^2, respectively. In all cases, the beam energies were chosen in order to have 212.3 MeV at the middle position of the target. Dashed lines display the results obtained with MOCADI_FUSION assuming the same interaction energy for all fusion events, while solid lines were calculated dividing the target thickness into thin bins and applying MOCADI_FUSION to each slice (FULL APPROACH). See text for additional details.

After the compound nucleus formation, PACE2 computes the probabilities for proton, neutron and α evaporation, for fission, for statistical γ emission and one of these possibilities is then chosen according to a Monte-Carlo calculation. The code subsequently calculates these probabilities for each intermediate nuclear species up to the final ER or to a fission event and determines the angular distribution of the ERs due to particle emission.

The original PACE2 version has been modified by inserting a proper subroutine to generate an output file

with the TRIM or ATIMA input file format. This file contains a list with all the fusion–evaporation events, and for each event the following information is included: ER mass (A) and atomic number (Z), energy (E), lateral (x) and vertical (y) position, remaining target thickness (z) (i.e. the difference between the whole target thickness and the depth at which the fusion process takes place) and three directional angles ($\cos\hat{x}$, $\cos\hat{y}$ and $\cos\hat{z}$). The reference frame is chosen with the z-axis along the beam direction and with the horizontal x-axis and vertical y-axis oriented as in a clock-wise system. The ER lateral and vertical coordinates, x and y, are calculated according to a two-dimensional Gaussian distribution with adjustable width and offset with respect to the optical axis. This width is assumed to be equal to the primary beam spot size, i.e. the angular straggling due to the atomic interaction of the projectiles with the target atoms prior to the fusion process is neglected. This is a reasonable approximation, since the kinematics of the ERs are mostly dominated by the kinematics of the fusion–evaporation process itself rather than by the small angular divergence of the primary beam.

2.2. Atomic interaction

A detailed knowledge of processes leading to atomic interaction with matter is crucial for an efficient tuning of the recoil separator. Atomic collisions with nuclei and electrons in the target, in possible degrader foils or vacuum windows typically lead to a slowing down and to an angular, energy and range (in case of stopped particles) straggling of the ERs.

In our scheme, the atomic interaction of the primary beam particles with the target atoms is considered assuming an interaction energy E_{int} (constant for all fusion events) smaller than the incident energy E_0. This assumption takes into account the slowing down of the projectiles in the target, whereas it neglects energy and angular straggling effects. However, these two phenomena have minor influences on the ER production cross section and kinematics, as already discussed in Section 2.1.

The atomic interaction of the ERs in the remaining target thickness between the nuclear interaction point and the target exit and in possible degraders is carried out either with the code ATIMA or TRIM. These programs calculate event-by-event the ER optical parameters, e.g. position vector, angles, mass, energy, and write them into a text file. These event data are eventually read by MOCADI as initial optical parameters [21]. In the energy range of the fusion–evaporation products ($E \leqslant 1$ MeV/μ) the use of TRIM or ATIMA is essentially equivalent, since ATIMA uses the TRIM algorithms to evaluate the energy lost in this energy domain.

Owing to the internal conversion and the subsequent rearrangement of the atomic shells, the ionic charge distributions (ICDs) of ERs recoiling out from the target are not equilibrated and therefore unpredictable. However, the knowledge of the mean charge state of the ERs is fundamental in order to achieve an efficient tuning of the all the ion-optical elements of the recoil separator. Thus, a thin carbon foil (30–60 μg/cm^2) is located downstream the target to restore the ICD equilibrium. Since fusion–evaporation reactions produce residues with rather wide energy spreads and the degree of ionization of ions passing through foils of matter depends on their atomic number and on their velocity, ERs typically have quite broad ICDs. For this reason, we inserted into the program which converts the TRIM (or ATIMA) output file into the MOCADI input file format, an appropriate Monte-Carlo subroutine to assign a charge state to each ER leaving the target. This procedure is done using the formula of Sagaidak and Yeremin [22], which is a slightly modified version of the systematics of Shima et al. [23].

2.3. Ion optics

The configuration and the ion-optical layout of a separator have to be adapted to the reaction kinematics and to the experimental goals. In case of fusion–evaporation reactions, the residues are typically produced with rather wide charge state and velocity distributions and with large angular spreads around the projectile direction. For primary beam energies smaller than 6 MeV/μ, the mean velocity of the ERs, v_{ER}, is rather close to that of the compound nucleus, v_{CN}. It is a fraction of the projectile velocity, v_{p}, according to the relation:

$$v_{\mathrm{ER}} \cong v_{\mathrm{CN}} = \frac{M_{\mathrm{p}}}{M_{\mathrm{p}} + M_{\mathrm{t}}} v_{\mathrm{p}} \tag{1}$$

where M_{p} and M_{t} are the projectile and the target mass, respectively. Therefore, charge-independent velocity filters generally provide an efficient separation between the ERs and the high intensity primary beam.

In MOCADI_FUSION the ion optics of the recoil separator used for the selection of the ERs is calculated with the program GICOSY [20]. This code uses the method of the transfer matrices. Each ion-optical element, i.e. a drift distance, a magnetic or electrostatic field sector, a magnetic or electrostatic multipole, a fringing field, is characterized by a transfer matrix. Matrices up to fifth order can be handled.

GICOSY is extremely flexible and allows the treatment of very complex experimental set-ups, the precise calculation of the fringing fields with the fringing field integral method and the use of variables and fitting procedures with different methods. The program finally creates the transfer matrices of all the ion-optical elements and these files are then included into the MOCADI input file and used for tracing the trajectories of the ERs and determining the evolution of their phase-space along the separator.

2.4. Fusion–evaporation reactions at SHIP

Since in the following section we will mainly apply the code MOCADI_FUSION to the velocity filter SHIP, we

now present as an example the ion-optical calculations performed for this recoil separator. However, the code can be easily adapted to other experimental set-ups because of its modular form.

The separator SHIP was commissioned at GSI in 1975. It has been widely used for the synthesis [6] and the spectroscopy [24] of super-heavy elements, for the discovery of the proton radioactivity [25] and for fusion reaction studies around [26] and far above the Coulomb barrier [27]. More recently, a double Penning trap system, SHIPTRAP [16], was installed behind the SHIP focal plane to perform precise mass measurements of nuclei along the *rp*-process [12], *n*-deficient nuclei in the rare-earth region close to the proton drip line, and super-heavy nuclides.

The ion-optical layout of SHIP is shown schematically in the upper part of Fig. 3. It consists of a quadrupole triplet (Q1–Q3), a two-stage velocity filter (E1–E2), a second quadrupole triplet (Q4–Q6) and a final dipole magnet (D5). The field arrangement inside the double Wien filter is the following: a high voltage condenser (E1) and two dipole magnets (D1–D2) for the first half, two more dipole magnets (D3–D4) and a high voltage condenser (E2) for the second part. A velocity slit (VS), with a variable opening of maximum ±23 mm (x-axis), is located at the middle position of the filter. The standard operation mode of SHIP is the field antisymmetric deflection mode with an intermediate focus. This configuration allows a better separation between the primary beam and the fusion–evaporation products at the velocity slits, because of the intermediate focus, and a higher transmission. The original set-up was extended by an additional dipole magnet (D5) in 1994. It provides a further background suppression of either low-energy primary beam particles passing through the filter with velocities similar to those of the ERs or high-energy projectiles, which are only slightly deflected by the filter because of their higher magnetic rigidity. This magnet is usually used at an angular deflection of 7.5° for spectroscopy experiments (see Fig. 3), also to screen the detectors from direct radiation from the target area, and at smaller deflection angles (2.5–3.5°) for stopping experiments, to achieve a somewhat higher transmission.

In our simulation, the fields for the electric sectors E1 and E2 and for the magnetic dipoles D1–D5 are determined directly from the mean kinetic energy (from PACE2 [17]), the mean charge state (according to the systematics of Sagaidak and Yeremin [22]) and the atomic mass (taken from the AME2003 [28]) of the desired ER. The pole-tip fields of the six quadrupole lenses are calculated with GICOSY by imposing two foci for both the dispersive direction, x, and the perpendicular coordinate, y. The intermediate focus is located at the velocity slit position between the D2 and D3 magnets, while the final focus can be placed either at the location of the SHIP focal plane detector system or at the SHIPTRAP stopping cell entrance window (see Fig. 3). For each quadrupole triplets a symmetric configuration is required, i.e. the field of the first lens is set equal to that of the third one. GICOSY then computes the transfer matrices (up to the third-order in the present case) of all the SHIP ion-optical elements. These matrices are finally combined in MOCADI together with the TRIM (or ATIMA) output data file to trace the ERs through the whole experimental set-up.

As an example, Fig. 3 presents several ER phase-space plots calculated with MOCADI at different locations along SHIP for the fusion–evaporation reaction ^{50}Ti (215 MeV) + ^{120}Sn (0.5 mg/cm^2) → ^{166}Hf + 4n. For each column of Fig. 3 we plotted the transverse emittances, (x, a) (top panel) and (y, b) (middle panel), and the energy-position correlation, (x, E) (bottom panel), where a and b are the angular coordinates for the horizontal (dispersive) direction, x, and the vertical axis, y, respectively.

The first column of Fig. 3 represents the phase-space distribution and the energy spread of a 215-MeV ^{50}Ti primary beam with an emittance of 8.3π mm mrad. The effects due to the fusion–evaporation reaction kinematics and to the atomic interaction of the ERs with the target electrons can be clearly seen in the second column of Fig. 3. The angular divergence and the energy spectrum of the ERs are nearly one order of magnitude broader than those for the primary beam, whereas the spatial distributions are rather similar. The third column of Fig. 3 describes the status of the ERs at the intermediate focal plane and the effects due to the velocity slits (vertical dashed lines). The choice of a ±23 mm opening for the x-slits is completely consistent with the full width at half maximum (FWHM) of the spatial distribution in the dispersive plane. Additionally, the distribution along the perpendicular axis (y-axis) is totally transmitted through the ±50 mm fixed aperture. The phase-space distributions at the final stage for both spectroscopy and stopping experiments are sketched in the fourth and fifth column of Fig. 3, respectively. The limits imposed by the size of the SHIP focal plane detector, 80 mm (x) × 35 mm (y), and by the SHIPTRAP gas cell entrance window, 30 mm radius, are indicated by the vertical dashed lines. These geometrical constraints are particularly severe in the second case, the number of transmitted ions being reduced by 25–30%.

Concerning the CPU time needed to run MOCADI_FUSION, for the reported example we used a PC with a 2 GHz processor and 2.99 GBytes of RAM. The simulation was carried out with 50,000 ^{166}Hf ERs, which required the generation of 200,000 fusion events with PACE2 in a running time of around 1.5 min. The evaluation of the atomic interaction of the ERs with the target atoms and the charge equilibration foil was performed with TRIM and took about 15 min. Finally, MOCADI needed less than 1 minute to trace the entire ensemble through SHIP. It resulted that the CPU time is mainly limited by the TRIM performances and that, within the range covered by our simulations, this time is scaling almost linearly with the target thickness and with the number of particles.

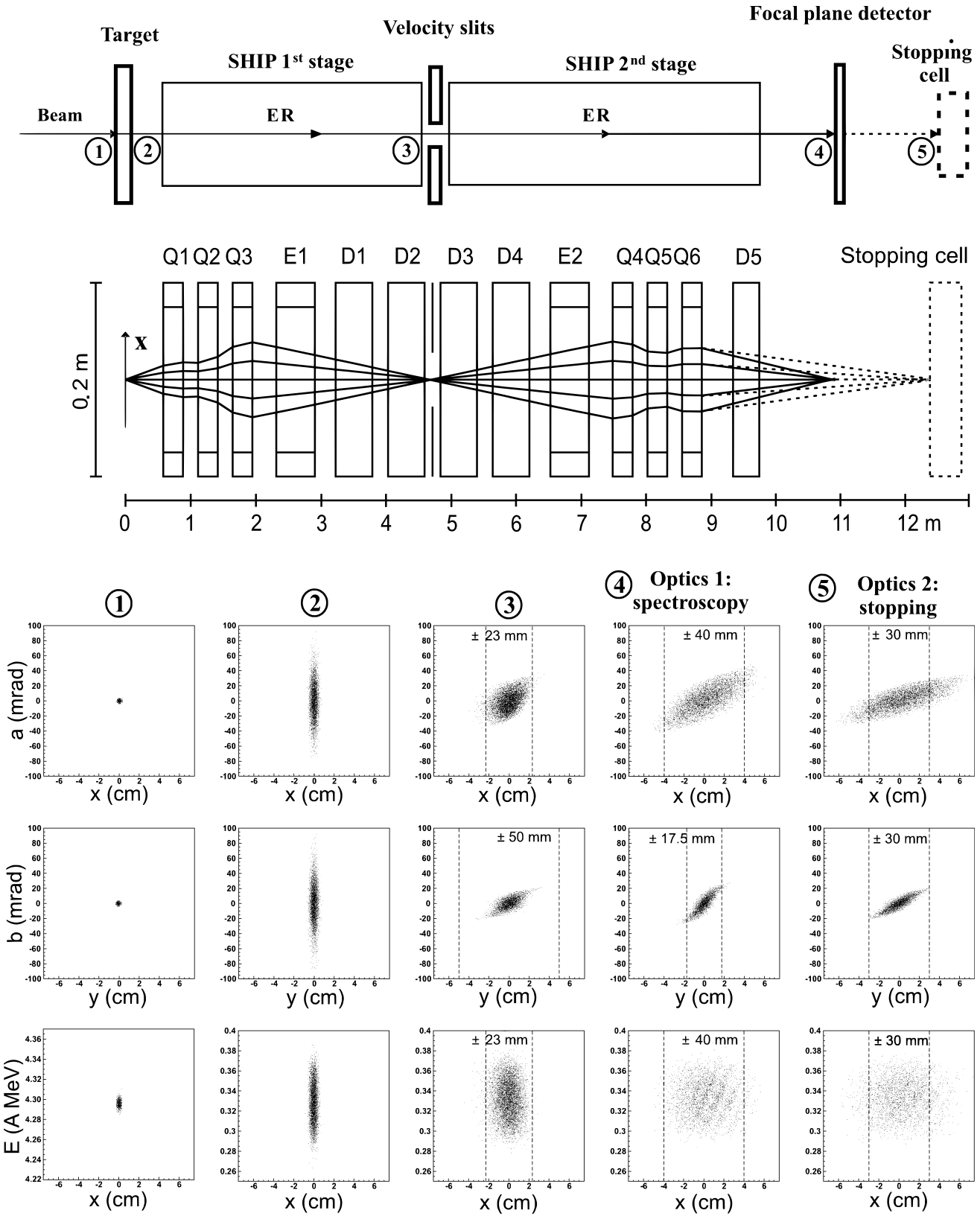

Fig. 3. Calculated transverse emittances and energy-position correlations of ^{50}Ti primary ions (column 1) and ^{166}Hf ERs (columns 2–5) produced in the reaction ^{50}Ti (215 MeV) + ^{120}Sn (0.5 mg/cm^2) at different locations along SHIP. The x-axis is the direction of the dispersion, y is perpendicular and a and b are the corresponding angular coordinates. The top panels show schematically the field arrangement of SHIP and the ion-optical trajectories through the separator. Vertical lines in columns 3–5 represent the opening of the velocity slits, the active area of the final focal plane detector and the entrance window of the SHIPTRAP gas cell, respectively. The calculations are done for a primary beam emittance of 8.3π mm mrad.

3. Applications to the production, separation and stopping of heavy-ion fusion reaction products

As a first application, MOCADI_FUSION has been applied to some fusion–evaporation reactions typically employed at the velocity filter SHIP. In this section we will first compare the PACE2 predictions with the experimental ER production cross sections for a test reaction (Section 3.1), in order to verify the reliability of our statistical model calculations. In Section 3.2, we will perform a comparative analysis of the MOCADI_FUSION predictions with the tabulated or, where available, experimental values for the transmission and the angular, charge state and velocity acceptances of SHIP. As a further application, we will use this code to estimate the range distribution of the ERs inside the SHIPTRAP stopping cell and to evaluate the efficiency of the whole SHIPTRAP apparatus (Section 3.3).

3.1. Evaporation residue production cross sections

Fig. 4 shows the comparison between the predictions of the statistical model code PACE2 [17] with the experimental values [29] for the production cross sections of 18 ERs in the fusion reaction ^{58}Ni (250 MeV) + ^{50}Cr (2 mg/cm^2). One can observe an overall quite good agreement between experimental and theoretical values, even if, according to the discussion carried out in Section 2.1, this is not the most favorable case to test the validity of our calculations. In fact, the target is rather thick and the primary beam loses 47.8 MeV (corresponding to 19% of its incident energy) passing through the target. Such a large energy loss does not allow us to assume that all fusion processes take place at the same interaction energy and that all the ER production cross sections have a rather constant or smooth behavior over an energy range of ~50 MeV. This fact is clearly responsible for the underestimation of the channels corresponding to the evaporation of a few particles (see Fig. 4). Indeed these cross sections are evaluated for a mean interaction energy higher than those corresponding to the maxima of the production cross sections for these ERs. However, the fact that an overall reasonable agreement with experimental data has been reached even for a rather thick target, supports even more strongly the approximation of a fixed interaction energy for thinner targets, at least at incident energies above the Coulomb barrier where the fusion cross section varies almost linearly with the beam energy. Comparisons with other complete (experimental) data sets of ER production cross sections for the same system at different energy [30] and for other systems leading to compound nuclei in the region around ^{100}Sn [31–33] gave similar results.

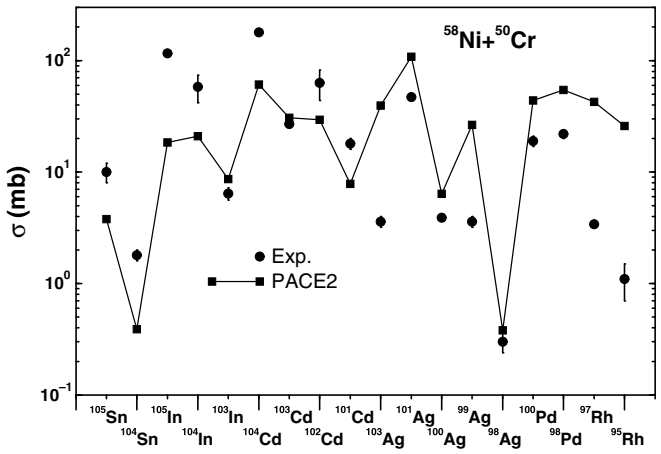

Fig. 4. Comparison between experimental values [29] and PACE2 predictions for the production cross sections of 18 ERs originating from the reaction ^{58}Ni (250 MeV) + ^{50}Cr (2 mg/cm^2). Calculated points are connected with straight lines to guide the eye.

We also notice that if we compare experimental and predicted values for each individual ER, the statistical model calculations can fail up to a factor of 10, e.g. for ^{103}Ag and ^{95}Rh. This indicates the level of confidence of our calculations: the overall behavior of the ER production cross sections is fairly reproduced, while the uncertainty for individual ER can be one order of magnitude. As the ERs approach the proton drip line, the proton, neutron and α separation energies are known only with large uncertainties (or they are simply extrapolated from the systematics, because of the lack or difficulty of precise mass measurements for such exotic nuclei). Thus, the poor knowledge of the basic nuclear properties limits the validity of the statistical model predictions in this region.

3.2. The transmission of the velocity filter SHIP

As a first test, the code MOCADI_FUSION was used to evaluate the transmission of the velocity filter SHIP for the reaction ^{40}Ar (186.4 MeV) + ^{175}Lu (0.469 mg/cm^2). The compound nucleus ^{215}Ac mainly decays via prompt fission, but also the α-emitter ^{211}Ac ($Q_\alpha = 7.621$ MeV, $E_\alpha = 7.472$ MeV, $t_{1/2} = 200(29)$ ms [34]) is populated via a quite large cross section of ≈60 μb [35] via a 4*n*-evaporation channel. We measured the detection rate and the position distribution of the 7.472-MeV α particles with the final focal plane detector of SHIP for different tuning settings of the separator ion-optical elements. From these quantities we derived the relative transmission of ^{211}Ac ions through SHIP and the centroids of their implantation profiles (see Fig. 5).

According to the MOCADI_FUSION predictions, ^{211}Ac ions recoil out from the target with an average velocity of $\langle v \rangle = 0.53$ cm/ns (which corresponds to a total kinetic energy of ≈30 MeV) and an ICD centered around the charge state $\langle q \rangle_{SAG} = 18+$ [22]. These values were used to define the "standard" tuning of the SHIP ion-optical elements. The settings were then recalculated for the same charge state ($\langle q \rangle_{SAG}$) but different velocities around the mean value (see Fig. 5(a)) and for the same average velocity (0.53 cm/ns) but different charge states (see Fig. 5(b) and (c)). For each setting we measured the rate and the horizontal position distribution in the SHIP final focal plane

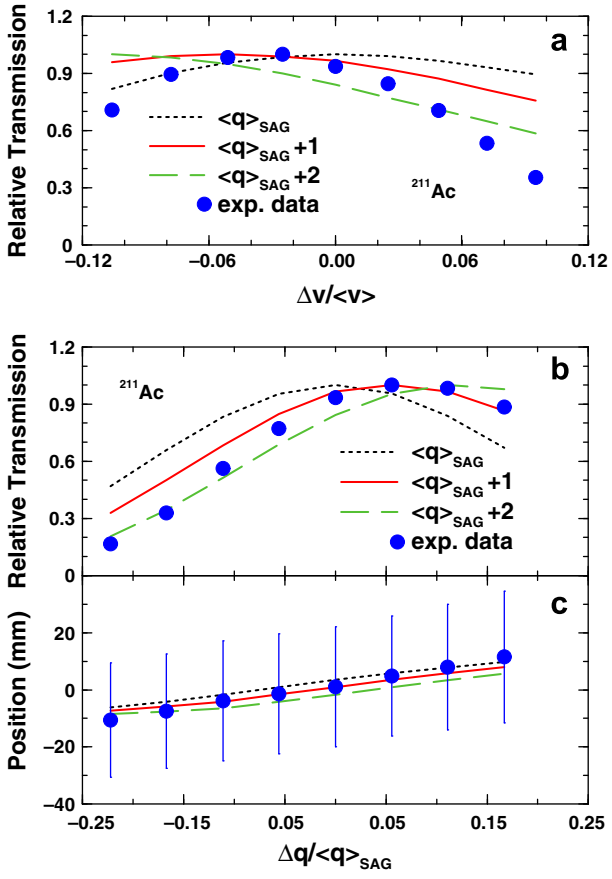

Fig. 5. Comparison between experimental and simulated data for the relative transmission through SHIP (upper and middle panel) and the centroids of the implantation profile at the SHIP final focal plane detector (lower panel) of ^{211}Ac ions produced in the reaction ^{40}Ar (186.4 MeV) + ^{175}Lu (0.469 mg/cm^2). Different points refer to different tuning settings for the ion-optical elements of SHIP (see text for additional details). Error bars are smaller than the symbols in panels (a) and (b), while they indicate the FWHMs of the implantation profiles in panel (c). Dotted, continuous and dashed curves are the results of the calculations done with MOCADI_FUSION assuming an ICD centered around the mean charge state predicted by the systematics of Sagaidak and Yeremin ($\langle q\rangle_{SAG} = 18+$), $\langle q\rangle_{SAG} + 1$ and $\langle q\rangle_{SAG} + 2$, respectively.

detector of the α particles from the decay of ^{211}Ac. Fig. 5 shows the comparison between experimental and simulated data for the ^{211}Ac relative transmission through SHIP (panels a and b) and the centroids of the implantation profiles (panel c). The calculations were iterated for ^{211}Ac ICDs centered at different mean charge states around the value predicted by the formula of Sagaidak and Yeremin, $\langle q\rangle_{SAG}$. We clearly see that a rather good agreement has been reached for an ICD shifted by one unit (continuous lines in Fig. 5) with respect to the systematics of Sagaidak and Yeremin. Such a deviation is still consistent with the level of accuracy of this systematics, stated by the authors within ±6% [22].

We also notice that MOCADI_FUSION predicts transmission distributions broader than the experimental data. This result indicates that the actual width of the ICD is probably slightly overestimated by the systematics of Sagaidak and Yeremin. In addition, the asymmetries between the right and left declines of the experimental data in Figs. 5(a) and 5(b) suggests that the use of a symmetric ICD is not totally adequate. More accurate measurements of the ICDs would be rather helpful to achieve a better agreement between experiment and simulation.

MOCADI_FUSION was also employed to estimate the absolute transmission through SHIP of different fusion–evaporation reactions. Fig. 6 shows the comparison between present results, experimental data and the transmission values calculated according to the procedures described in [36,37]. Data have been plotted versus the ratio between the projectile and the target masses. The simulated values were optimized in order to achieve the maximum production yield for the selected ER, i.e. we maximized the product of the target thickness and the transmission of the ER through SHIP.

The available experimental values are rather well reproduced by MOCADI_FUSION. Agreements within ∼16% and ∼9% have been reached for the reactions ^{50}Ti (215 MeV) + ^{120}Sn (0.5 mg/cm^2) (→ ^{170}Hf*) → ^{166}Hf + 4n, and ^{12}C (60 MeV) + ^{142}Nd (0.218 mg/cm^2) (→ ^{154}Dy*) → ^{151}Dy + 3n, respectively.

The comparison with the other estimates of the SHIP transmission is also quite relevant, in particular if we consider that two different procedures were employed for the calculation of the SHIP ion optics. In our case, a symmetric configuration of both quadrupole triplets together with an intermediate (final) focus at the velocity slits (SHIP final focal plane) was required. The other approach optimized the optics of the first (second) quadrupole triplet by maximizing the ER transmission at the exit of the velocity filter (on the surface of the focal plane detector), without requiring any focusing conditions. Moreover, two different methods were used to evaluate the ER mean charge state: in our

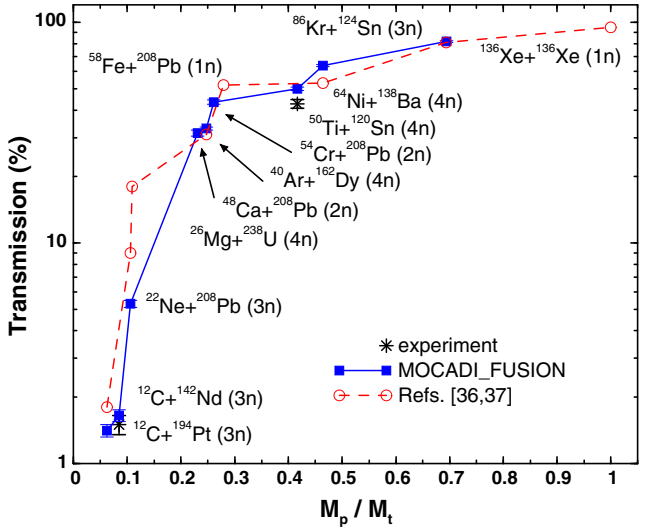

Fig. 6. Comparison between the experimental transmission of the velocity filter SHIP, that calculated employing the code MOCADI_FUSION (present work) and that obtained according to the procedure described in [36,37].

case the formula of Sagaidak and Yeremin [22] was employed, whereas the other used the systematics of Nikolaev and Dmitriev [38]. We can deduce from Fig. 6 that the second procedure provides a higher transmission in case of very mass-asymmetric reactions, while both predictions coincide for the reaction ^{40}Ar (173 MeV) + ^{162}Sn (0.25 mg/cm^2) → ^{198}Po + 4n. For more symmetric reactions, our estimates provide a slightly larger transmission.

Finally, Fig. 6 shows that the transmission decreases as the mass asymmetry ratio between projectile and target increases. This is due to recoil and atomic interaction effects, which are much larger for reactions induced from light projectiles on heavy targets, because of the smaller compound nucleus velocity. The role played by the neutron evaporation on the transmission along the different sections of SHIP will be discussed in Section 3.2.1, while the case of α and proton evaporation will be covered in Section 3.3.1.

3.2.1. Angular acceptance of SHIP

MOCADI_FUSION has been lastly used to evaluate the angular, charge state and velocity acceptances of SHIP. These three quantities are strongly interconnected to each other, in particular charge and velocity selections. However, in the following discussion, we will try to treat individually the different acceptances and to compare our results with those previously estimated [39]. We will consider three reactions with different ratios between the masses of the projectile and the target: the two reactions for which experimental data are presently available, i.e. ^{12}C + ^{142}Nd → ^{151}Dy + 3n (reaction I, large mass-asymmetry, $M_p/M_t = 0.08$) and ^{50}Ti + ^{120}Sn → ^{166}Hf + 4n (reaction II, medium mass-asymmetry, $M_p/M_t = 0.42$), and the more symmetric reaction ^{86}Kr (350 MeV) + ^{124}Sn (0.5 mg/cm^2) → ^{207}Rn + 3n (reaction III).

Fig. 7 shows the transmission along SHIP for the three fusion–evaporation reactions considered. The ERs produced in these reactions recoil out from the target with different angular spreads. The FWHMs of the angular divergences at the target exit for ^{151}Dy, ^{166}Hf and ^{207}Rn ions are 517 mrad (29.6°), 92 mrad (5.3°) and 49 mrad (2.8°), respectively. This feature is clearly connected to the transmission through the separator: the larger the angular divergence of the ERs at the target exit, the smaller the transmission through SHIP. This effect is particularly evident at the exit of the first quadrupole triplet (Q1–Q3). In fact, whereas ~95% (70%) of ^{207}Rn (^{166}Hf) ions pass through the first three ion-optical elements of SHIP, only ~7% of ^{151}Dy ERs are transmitted to the entrance of the first electric sector (E1). The velocity slits (VS) together with the velocity dispersion introduced by the double Wien filter, which is strongly related to the transmission losses inside the second quadrupole triplet (Q4–Q6), further reduce the number of transmitted ions. Finally the last dipole magnet (D5) and the finite size of the SHIP final focal plane detector provide an additional 10% reduction of the total transmission.

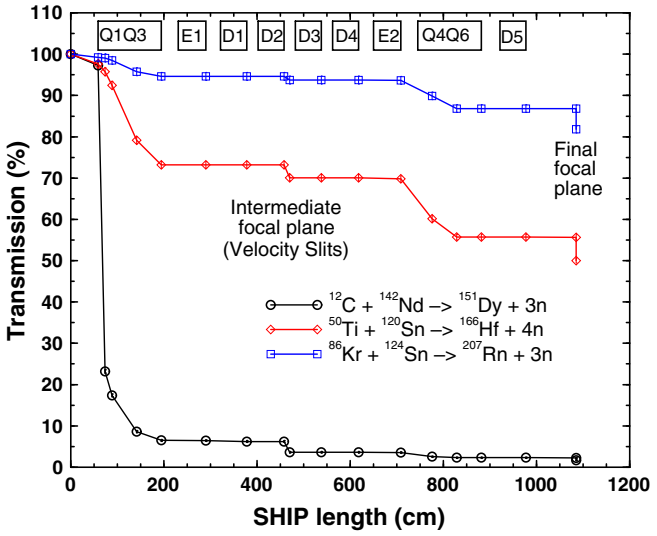

Fig. 7. Calculated transmission at different locations along the velocity filter SHIP for three heavy-ion fusion–evaporation reactions with different mass-asymmetry. Boxes represent the geometrical lengths of the ion-optical elements of SHIP.

These studies allow to evaluate the solid angle coverage of SHIP. Our estimates for the horizontal ($\Delta\theta = \pm 35$ mrad) and vertical ($\Delta\phi = \pm 30$ mrad) acceptances lead to a solid angle coverage of ~3.3 msr. This value is slightly larger than that reported for the original configuration of SHIP (2.7 msr [15,39]), since it takes into account the new layout of the separator (modified in 1994) with the target closer to the entrance of the first quadrupole magnet Q1 [6].

3.2.2. Charge state acceptance of SHIP

As discussed in Section 2.2, ERs are usually produced with rather broad ICDs. Thus, in order to achieve the highest possible transmission, the use of charge-independent filters is frequently undertaken. However, the maximum deviation in charge from the charge state that the separator was tuned to ($\langle q \rangle$), is limited by the deflections in the electric and magnetic fields of the optical elements. In our case, an accepted charge width $\Delta q/\langle q \rangle = \pm 10\%$ was reported for the velocity filter SHIP [39].

Fig. 8 shows the ICDs at the entrance of SHIP (solid curves) and at the final focal plane detector (dotted curves) for the three fusion–evaporation reactions already considered. We clearly see that ^{207}Rn and ^{166}Hf ions are produced with initial ICDs within the accepted charge width of the separator (horizontal arrows in Fig. 8). Thus no relevant effect arising from the charge selection is expected for these ERs. Our simulation, in fact, predicts final ICDs as broad as the initial ones. The reduced number of transmitted ions is mainly due to the angular acceptance of the separator (see Section 3.2.1), since, as we will see in Section 3.2.3, ^{207}Rn and ^{166}Hf have velocity distributions smaller than the velocity width accepted by SHIP.

In the case of reaction I, ^{151}Dy ions are generated with very broad angular (see Section 3.2.1), charge state (see Fig. 8(a)) and velocity (see Fig. 9(a)) distributions. In

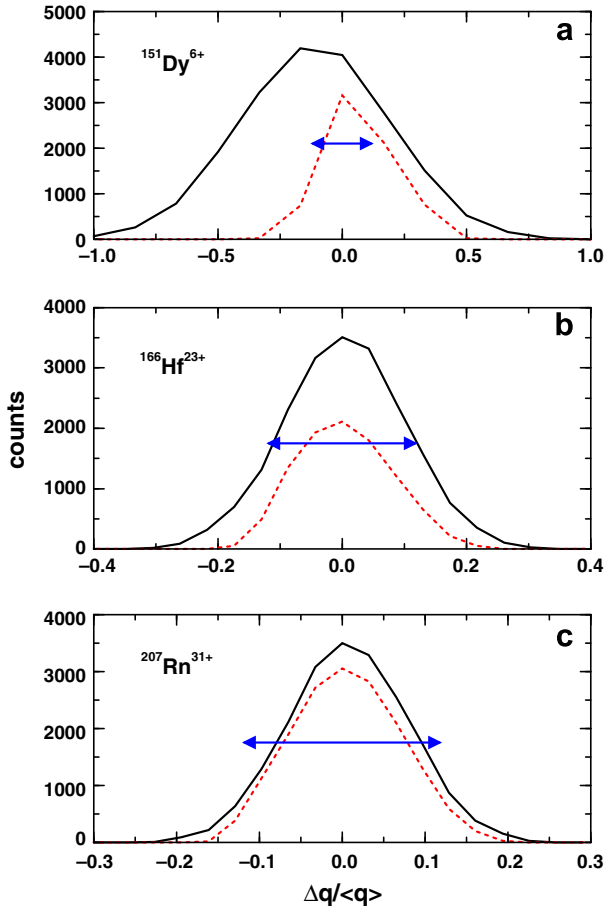

Fig. 8. Calculated ICDs for three ERs produced in fusion reactions with different mass-asymmetry ratios. Black continuous and red dotted curves describes the charge state distributions at the entrance of SHIP and at the final focal plane detector, respectively. The red dotted curve in panel a is multiplied by 20. Horizontal arrows indicate a charge state acceptance of ±10% around the charge states employed for the tuning of the ion-optical elements of SHIP. (For interpretation of the references to colour in this figure legend, the reader is referred to the web version of this article.)

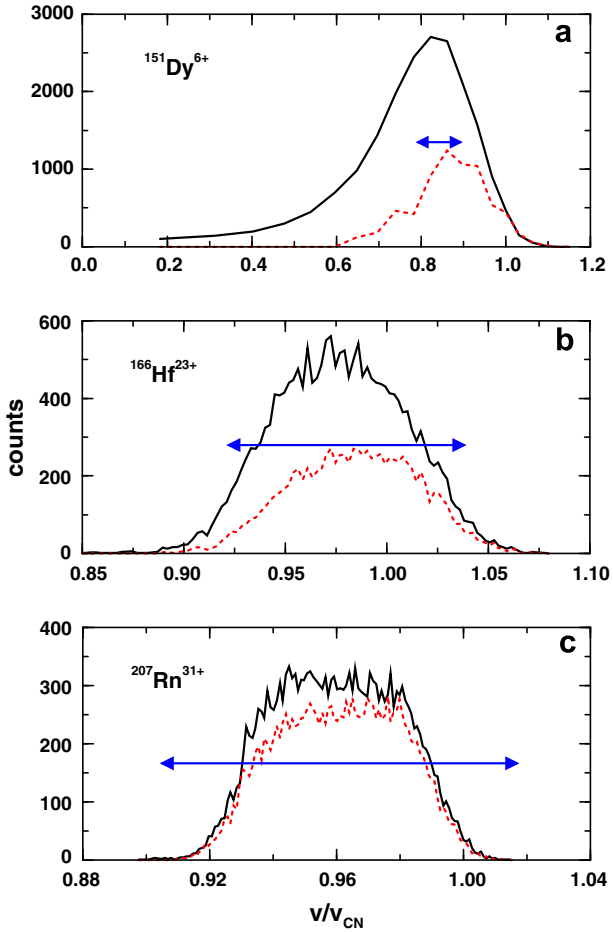

Fig. 9. Calculated velocity spectra for three ERs produced in fusion reactions with different mass-asymmetry ratios. Black continuous and red dotted curves refer to the velocity spectra at the entrance of SHIP and at the final focal plane detector, respectively. Data are plotted versus the ratio v/v_{CN}. The red dotted curve in the upper panel is multiplied by 20. Horizontal arrows indicate a velocity acceptance of ±5% around the value used for the tuning of the ion-optical elements of SHIP. (For interpretation of the references to colour in this figure legend, the reader is referred to the web version of this article.)

particular, the ICD is at least a factor 3 wider than the charge width accepted by SHIP, therefore a rather large charge state selection is expected for these ERs. MOCADI_FUSION computes a final ICD centered around the charge state used for the tuning of SHIP and with a width compatible with a charge state acceptance $\Delta q/\langle q\rangle = \pm 10\%$, as previously estimated [39].

3.2.3. Velocity acceptance of SHIP

We finally employed MOCADI_FUSION to study the velocity width accepted by SHIP. Also in this case we considered the three reactions already mentioned (see Fig. 9). The scenario is rather similar to that discussed in Section 3.2.2 for the charge state acceptance of SHIP. In fact ^{207}Rn and ^{166}Hf ERs have initial velocity spreads smaller than the range accepted by SHIP, $\Delta v/\langle v\rangle = \pm 5\%$ [39] (horizontal arrows in Fig. 9) and no velocity selection is expected for these ions. Indeed our code predicts just a partial suppression of the ^{166}Hf and ^{207}Rn low-velocity tails. We thus conclude that for reactions II and III the selection of the ERs and, consequently, their transmission are mostly dominated by the angular acceptance of SHIP.

The situation is different for ^{151}Dy ions since their velocity distribution is rather broad. In this case, as already observed in Section 3.2.2, we have a simultaneous selection due to the combined action of velocity, charge state and angular acceptances, whose effects are quite difficult to disentangle. Our code foresees a final velocity spectrum centered at a value slightly higher than the ER initial mean velocity, which was employed for the tuning of the separator, and with a FWHM (±6.5%) a bit larger than the tabulated velocity acceptance of SHIP [39].

3.3. Experiments at SHIPTRAP

After its development and the study of basic features, the code MOCADI_FUSION has also been used for the preparation and the analysis of experiments performed at

SHIPTRAP [16] in the period February 2006–June 2007. In these experiments, whose aim is precision mass measurements, the ERs are first separated from the primary beam by the velocity filter SHIP and then enter a helium-filled gas cell through a few μm thick titanium foil. The ions are thermalized by atomic collisions with the gas inside the cell and then dragged by a combination of electrical DC and radio frequency (RF) fields towards a nozzle, where they are swept out by a supersonic gas jet into an extraction RF-quadrupole. The ERs are then cooled, bunched and finally injected into a first Penning trap (purification trap), which acts as an isobar separator. A second Penning trap (measurement trap) is employed to perform high-precision mass measurement.

MOCADI_FUSION was employed for the reactions ^{40}Ca, ^{50}Cr, ^{58}Ni + ^{58}Ni [40–42] to help accomplish the following tasks: (i) to optimize several experimental parameters, such as target/projectile combination, primary beam energy, target thickness and SHIP ion-optical setting, in order to achieve the highest yields of ERs in the mass region close to the expected end-point of the *rp*-process [12]; (ii) to estimate the isobaric contaminations; (iii) to evaluate the transmission of the ERs through SHIP and (iv) to determine the thickness of the mylar degrader foils to be placed in front of the SHIPTRAP gas-cell entrance window, in order to optimize the matching between the residual range of the ERs in helium gas and the gas-cell extraction region.

As an application, we will present briefly in this section some criteria to identify the most suitable fusion–evaporation reactions to access very exotic nuclei (Section 3.3.1), the calculation of the residual range of the ERs into the SHIPTRAP gas cell (Section 3.3.2) and the experimental SHIPTRAP efficiency (Section 3.3.3). We will finally discuss the actual possibilities to perform direct mass measurements of transfermium nuclei at SHIPTRAP.

3.3.1. Criteria for the choice of the most suitable fusion–evaporation reaction

Fig. 10 shows the relation between the angular divergence at the target exit and the transmission through SHIP for thirteen ERs produced in the reaction ^{50}Cr (180 MeV) + ^{58}Ni (0.5 mg/cm^2). The data points can be separated into three regions, according to their production evaporation chain. ERs produced only via proton and/or neutron evaporation are characterized by a lower angular divergence and a higher transmission. If an α particle has been evaporated in addition, the recoil effects are larger and the corresponding ERs turn out to have a wider angular divergence and a smaller transmission through the separator. The ER which corresponds to the 2α*p*-evaporation chain, has an even wider divergence, but its transmission is comparable with those for the 1α*xpyn* channels. We have already noticed in Section 3.2.1 that the lower the angular divergence is, the higher the SHIP transmission. However, we clearly see that the transmission does not significantly decrease going from the 1α evaporation channels to the 2α one. This is because in both cases the ERs have angular spreads exceeding the SHIP angular acceptance (see Section 3.2.1), thus the dependence of the transmission on the angular divergence of the ERs at the target exit gets weaker.

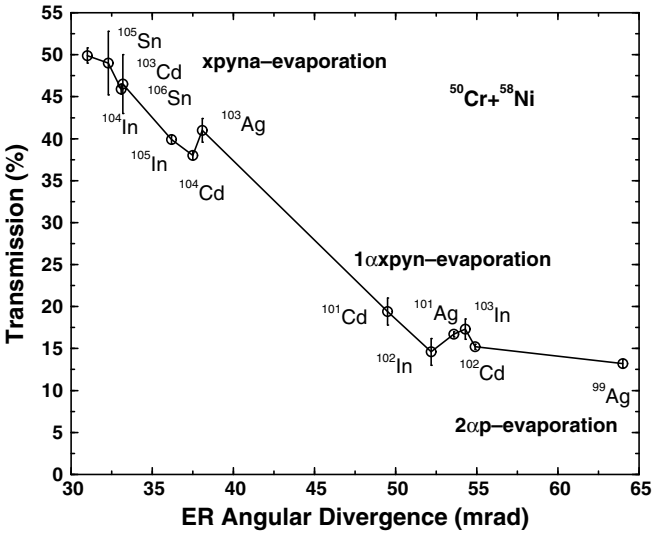

Fig. 10. Calculated transmission through SHIP versus the angular divergence at the target exit for the main ERs produced in the reaction ^{50}Cr (180 MeV) + ^{58}Ni (0.5 mg/cm^2).

This feature indicates a doorway to access exotic nuclei via fusion–evaporation reactions avoiding strong contaminations from ERs populated via α particle evaporation. In fact, let us assume that the same ER can be produced with similar cross sections via two reactions: in the first case only via proton and/or neutron evaporation and in the other one also via emission of at least one α particle. In such a case, the former reaction should be preferred over the latter, since it allows for a higher transmission of the selected species and it provides an additional suppression of contaminating ERs produced via α evaporation.

3.3.2. ER range distributions in the SHIPTRAP stopping cell

In order to achieve the highest stopping efficiency inside the gas cell, the residual range of the ERs in helium gas should match the SHIPTRAP extraction region [43]. This zone corresponds to the inner part of a DC cage made up by a set of five cylindrical grid electrodes with a diameter of 16 cm. The center of the cage is located 18 cm behind the thin titanium gas cell entrance foil. A DC electrical field is applied to the electrodes and guides the ions towards the radio frequency DC funnel, from where they are transferred to the nozzle. The gas cell is typically working at a pressure of 40–50 mbar and at room temperature.

Fig. 11 upper panel shows the calculated residual range in helium for ^{166}Hf and ^{207}Rn ions produced in the fusion–evaporation reactions ^{50}Ti (215 MeV) + ^{120}Sn (0.5 mg/cm^2) and ^{86}Kr (350 MeV) + ^{124}Sn (0.5 mg/cm^2), respectively. Although the ERs loose a large fraction of their

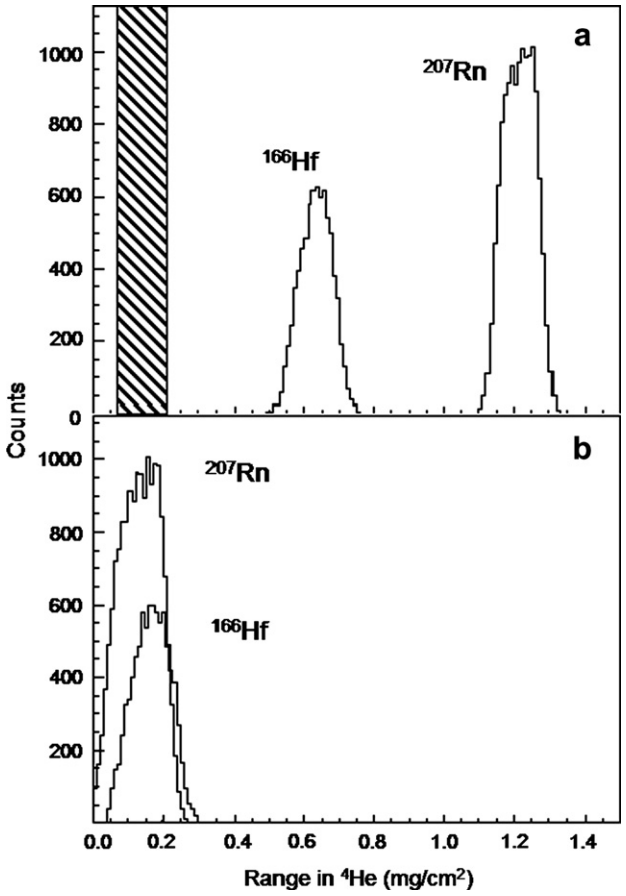

Fig. 11. Upper panel: calculated residual range in helium for ^{166}Hf and ^{207}Rn ions produced in the fusion–evaporation reactions ^{50}Ti (215 MeV) + ^{120}Sn (0.5 mg/cm^2) and ^{86}Kr (350 MeV) + ^{124}Sn (0.5 mg/cm^2), respectively. The hatched area represents the extraction region of the SHIPTRAP gas cell for a helium gas pressure of 50 mbar at room temperature. Lower panel: same as in the upper panel after the ^{166}Hf and ^{207}Rn residues have passed through an additional mylar degrader thickness of 4 μm and 10 μm, respectively.

kinetic energies in the 3.3 μm thick Ti-entrance window, the residual ranges are still exceeding by far the SHIPTRAP extraction region (indicated in Fig. 11(a) with a hatched area). Thus, additional degrader foils have to be placed in front of the Ti-window in order to slow down the ERs to an adequate kinetic energy and to maximize the overlap between the residual range distribution of the ERs and the SHIPTRAP gas cell extraction region. MOCADI_FUSION has proved to be useful for the prediction of the proper thickness of the degrader foils. As an example, for the two reactions considered, mylar thicknesses of 4 μm and 10 μm, respectively, would be required to maximize the ^{166}Hf and ^{207}Rn extraction efficiency from the gas cell (see Fig. 11(b)).

3.3.3. SHIPTRAP overall efficiency

The knowledge of the SHIP transmission enables us to evaluate the overall SHIPTRAP efficiency quantitatively. Here, we define the efficiency as the ratio between the measured number of ions impinging on the SHIPTRAP Micro

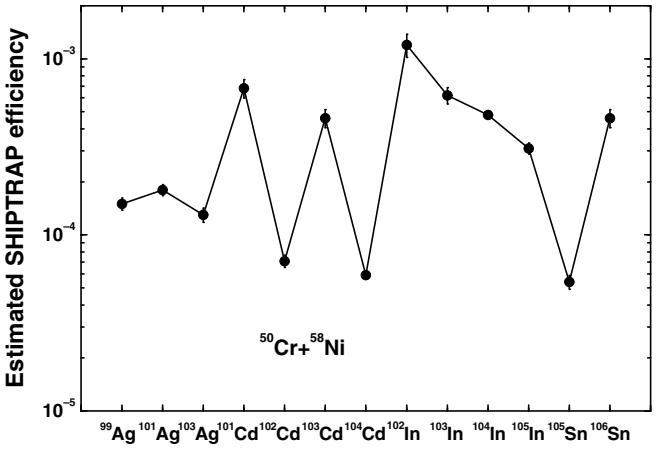

Fig. 12. Overall SHIPTRAP efficiency (see text) for the main ERs produced in the reaction ^{50}Cr + ^{58}Ni at 180 MeV beam energy. Plotted errors are only statistical. Experimental points are connected with straight lines to guide to eye.

Channel Plate (MCP) detector located behind the measurement trap and the calculated number of ions entering the stopping cell entrance window. Of course SHIPTRAP consists of several sections (stopping cell, DC cage, RF–DC funnel, extraction RF quadrupole, cooler, buncher, transfer, purification trap, measurement trap, focal plane detector), each of them with its own efficiency, thus, giving its own contribution to the overall SHIPTRAP efficiency. We determined this quantity for the main ERs produced in the reaction ^{50}Cr (180 MeV) + ^{58}Ni (0.5 mg/cm^2) (see Fig. 12). For each ER, we measured the ratio between the number of ions detected at the end of the set-up with respect to those (calculated) entering the SHIPTRAP gas cell. The latter number was estimated starting from the PACE2 production cross section, the SHIP transmission provided by MOCADI_FUSION, the target thickness and the average primary beam current.

The SHIPTRAP overall efficiency was expected to be rather similar for all ERs, at least for different isotopes of the same element. In fact, since the chemical properties employed for the extraction from the gas cell could vary from element to element, one may expect different extraction efficiencies for different elements. Fig. 12 shows that for silver and, within a factor 3, indium isotopes, we obtained rather similar efficiencies, while cadmium and tin isotopes exhibit variations larger than one order of magnitude. The only source of uncertainty which can account for such large deviations is the estimate of ER production cross section. In Section 3.1, in fact, we pointed out that PACE2 reproduces quite well the overall trend of the ER experimental cross sections, but for each individual species the prediction can differ up to a factor 10, as shown in Fig. 4.

However, we can extract from the data an average value for the overall SHIPTRAP efficiency, which turns out to be $\sim 4 \times 10^{-4}$. This value has a crucial relevance in order to establish the lowest accessible ER production cross section, for which a high-precision mass measurement could be

undertaken at present. Considering that up to now cross sections down to tens of μb have been measured with a relative mass precision as low as 5×10^{-8} [44,45], a first direct mass measurement in the transfermium region should be feasible in the near future. The best candidate is ^{254}No, which is produced with a cross section of 2.2 μb via the fusion–evaporation reaction $^{48}Ca + ^{208}Pb \rightarrow ^{254}No + 2n$ [46]. Assuming a primary beam current of 1.5 pμA, a target thickness of 0.5 mg/cm^2, a SHIP transmission of ~30% and the future improvements foreseen at SHIPTRAP [47], a trap resonance with $N = 300$ ions, which corresponds to a statistical mass uncertainty of about 22 keV [47], should be measured in about 5 h.

4. Conclusions

The Monte-Carlo code MOCADI, originally developed for high-energy fission and fragmentation reactions, has been extended to heavy-ion fusion–evaporation reactions. As a first utilization, the program has been applied to the velocity filter SHIP at GSI. It has shown a quite good agreement with the available experimental data for the relative transmission of SHIP and it has fairly reproduced the angular, charge state and velocity acceptances of SHIP. The program has been also used for the optimization of suitable projectile–target combinations and beam energies for precise mass measurements of nuclei involved in the stellar *rp*-process at the double Penning trap system SHIPTRAP and to evaluate the overall efficiency of SHIPTRAP.

For the future we aim at exploiting the code and its capabilities for other experimental set-ups where heavy-ion fusion–evaporation reactions are employed, such as the Fragment Mass Analyzer (FMA) [48] at Argonne (USA) and the Recoil Mass Spectrometer (RMS) [49] at Oak Ridge (USA), and to apply the program for direct mass measurements in the transfermium region at SHIPTRAP. Recently we have successfully extended the code by including also the reaction kinematics of low-energy two-body direct processes [50], such as those employed at the EXOTIC facility [51] of the Laboratori Nazionali di Legnaro (Italy) for the in-flight production of light weakly-bound Radioactive Ion Beams.

Acknowledgement

The authors warmly thank D. Boutin, C. Kozhuharov, D. Pierroutsakou, C.Signorini and J. Winfield for carefully reading the manuscript and for many fruitful discussions and suggestions. This work was partially supported by the Helmholtz Association and GSI under VH-NG-033 and by the BMBF under Contract No. 06GI185I.

References

[1] N. Iwasa, H. Geissel, G. Münzenberg, C. Scheidenberger, Th. Schwab, H. Wollnik, Nucl. Instr. and Meth. B 126 (1997) 284.
[2] H. Geissel, P. Armbruster, K.H. Behr, A. Brünle, K. Burkard, M. Chen, H. Folger, B. Franczak, H. Keller, O. Klepper, B. Langenbeck, F. Nickel, E. Pfeng, M. Pfützner, E. Roeckl, K. Rykaczewski, I. Schall, D. Schardt, C. Scheidenberger, K.-H. Schmidt, A. Schröter, T. Schwab, K. Smmerer, M. Weber, G. Münzenberg, Nucl. Instr. and Meth. B 70 (1992) 286.
[3] B. Franzke, Nucl. Instr. and Meth. B 24–25 (1987) 18.
[4] H. Geissel, H. Weick, M. Winkler, G. Münzenberg, V. Chichkine, M. Yavor, T. Aumann, K.H. Behr, M. Böhmer, A. Brünle, K. Burkard, J. Benlliure, D. Cortina-Gil, L. Chulkov, A. Dael, J.-E. Ducret, H. Emling, B. Franczak, J. Friese, B. Gastineau, J. Gerl, R. Gernhäuser, M. Hellström, B. Jonson, J. Kojouharova, R. Kulessa, B. Kindler, N. Kurz, B. Lommel, W. Mittig, G. Moritz, C. Mühle, J.A. Nolen, G. Nyman, P. Roussell-Chomaz, C. Scheidenberger, K.-H. Schmidt, G. Schrieder, B.M. Sherrill, H. Simon, K. Sümmerer, N.A. Tahir, V. Vysotsky, H. Wollnik, A.F. Zeller, Nucl. Instr. and Meth. B 204 (2003) 71.
[5] W. Henning, Nucl. Phys. A 734 (2004) 654.
[6] S. Hofmann, G. Münzenberg, Rev. Mod. Phys. 72 (2000) 733.
[7] A. Gillitzer, T. Fästermann, K. Hartel, P. Kienle, E. Nolte, Z. Phys. A 326 (1987) 107.
[8] R.D. Page, P.J. Woods, R.A. Cunningham, T. Davinson, N.J. Davis, A.N. James, K. Livingston, P.J. Sellin, A.C. Shotter, Phys. Rev. C 49 (1994) 3312.
[9] I. Mukha, E. Roeckl, L. Batist, A. Blazhev, J. Döring, H. Grawe, L. Grigorenko, M. Huyse, Z. Janas, R. Kirchner, M. La Commara, C. Mazzocchi, S.L. Tabor, P. Van Duppen, Nature 439 (2006) 298.
[10] J. Gomez del Campo, C. Baktash, H.-Q. Jin, D. Rudolph, A. D'Onofrio, F. Terrasi, G. De Angelis, M. De Poli, C. Fahlander, A. Gadea, D.R. Napoli, Q. Pan, P. Spolaore, L. De Acuna, D. Bazzacco, S. Lunardi, P. Pavan, C. Rossi-Alvarez, A. Buscemi, R. Zanon, A. De Rosa, L. Campajola, M. La Commara, G. Inglima, V. Roca, M. Romano, M. Sandoli, M. Romoli, A. Ordine, D. Pierroutsakou, Phys. Rev. C 57 (1998) R457.
[11] M. Kavatsyuk, L. Batist, F. Becker, A. Blazhev, W. Brüchle, J. Döring, T. Fästermann, M. Górska, H. Grawe, Z. Janas, A. Jungclaus, M. Karny, O. Kavatsyuk, R. Kirchner, M. La Commara, S. Mandal, C. Mazzocchi, I. Mukha, S. Muralithar, C. Plettner, A. Plochocki, E. Roeckl, M. Romoli, M. Schädel, J. Zylic, Eur. Phys. J. A 29 (2006) 183.
[12] H. Schatz, A. Aprahamian, J. Gorres, M. Wiescher, T. Rauscher, J.F. Rembges, F.-K. Thielemann, B. Pfeiffer, P. Moller, K.-L. Kratz, H. Herndl, B.A. Brown, H. Rebel, Phys. Rep. 294 (1998) 167.
[13] O.B. Tarasov, D. Bazin, Nucl. Instr. and Meth. B 204 (2003) 174.
[14] D. Bazin, O. Tarasov, M. Lewitowicz, O. Sorlin, Nucl. Instr. and Meth. A 482 (2002) 307;
O.B. Tarasov, D. Bazin, Nucl. Phys. A 746 (2004) 411c.
[15] G. Münzenberg, W. Faust, S. Hofmann, P. Armbruster, K. Güttner, H. Ewald, Nucl. Instr. and Meth. Phys. Res. 161 (1979) 65.
[16] M. Block, D. Ackermann, D. Beck, K. Blaum, M. Breitenfeldt, A. Chauduri, A. Doemer, S. Eliseev, D. Habs, S. Heinz, F. Herfurth, F.P. Heßberger, S. Hofmann, H. Geissel, H.-J. Kluge, V. Kolhinen, G. Marx, J.B. Neumayr, M. Mukherjee, M. Petrick, W. Plaß, W. Quint, S. Rahaman, C. Rauth, D. Rodríguez, C. Scheidenberger, L. Schweikhard, M. Suhonen, P.G. Thirolf, Z. Wang, C. Weber, the SHIPTRAP Collaboration, Eur. Phys. J. A 25 (Suppl. 1) (2005) 49.
[17] A. Gavron, Phys. Rev. C 21 (1980) 230.
[18] C. Scheidenberger, H. Geissel, Th. Stöhlker, H. Folger, H. Irnich, C. Kozhuharov, A. Magel, P.H. Mokler, R. Moshammer, G. Münzenberg, F. Nickel, M. Pfützner, P. Rymuza, W. Schwab, J. Ullrich, B. Voss, Nucl. Instr. and Meth. B 90 (1994) 36.
[19] J.F. Ziegler, <http://www.srim.org>.
[20] M. Berz, H.C. Hoffmann, H. Wollnik, Nucl. Instr. and Meth. A 258 (1987) 402.
[21] MOCADI manual: <http://www-linux.gsi.de/~weick/mocadi/mocadi-manual.html>.
[22] R.N. Sagaidak, A.V. Yeremin, Nucl. Instr. and Meth. B 93 (1994) 103.

[23] K. Shima, T. Ishihara, T. Mikumo, Nucl. Instr. and Meth. Phys. Res. 200 (1982) 605.
[24] M. Leino, F.P. Heßberger, Ann. Rev. Nucl. Part. Sci. 54 (2004) 175.
[25] S. Hofmann, W. Reisdorf, G. Münzenberg, F.P. Heßberger, J.R.H. Schneider, P. Armbruster, Z. Phys. A 305 (1982) 111.
[26] W. Reisdorf, F.P. Heßberger, K.D. Hildenbrand, S. Hofmann, G. Münzenberg, K.-H. Schmidt, J.H.R. Schneider, W.F.W. Schneider, K. Sümmerer, G. Wirth, J.V. Kratz, K. Schlitt, Nucl. Phys. A 438 (1985) 212.
[27] F.P. Heßberger, V. Ninov, S. Hofmann, D. Ackermann, S. Saro, M. Veselsky, Z. Phys. A 348 (1994) 301.
[28] G. Audi, O. Bersillon, J. Blachot, A.H. Wapstra, Nucl. Phys. A 729 (2003) 3.
[29] R. Schubart, H. Grawe, J. Heese, H. Kluge, K.H. Maier, M. Schramm, Z. Phys. A 352 (1995) 373.
[30] H. Grawe, M. Górska, M. Lipoglavšek, R. Schubart, A. Atac, A. Axelsson, J. Blomqvist, J. Cederkall, G. De Angelis, M. De Poli, C. Fahlander, A. Johnson, K.H. Maier, L.-O. Norlin, J. Nyberg, D. Foltescu, M. Palacz, J. Persson, M. Rejmund, H.A. Roth, T. Shizuma, O. Skeppstedt, G. Sletten, M. Weiszflog, the OSIRIS/NORDBALL-PEX/EUROBALL Collaboration, Z. Phys. A 358 (1997) 185.
[31] M. Górska, H. Grawe, D. Kast, G. De Angelis, P.G. Bizzeti, B.A. Brown, A. Dewald, C. Fahlander, A. Gadea, A. Jungclaus, K.P. Lieb, K.H. Maier, D.R. Napoli, Q. Pan, R. Peusquens, M. De Poli, M. Rejmund, H. Tiesler, Phys. Rev. C 58 (1998) 108.
[32] M. Lipoglavšek, M. Górska, J. Nyberg, A. Atac, A. Axelsson, R.A. Bark, J. Blomqvist, J. Cederkall, B. Cederwall, G. De Angelis, C. Fahlander, H. Grawe, A. Johnson, S. Leoni, A. Likar, M. Matiuzzi, S. Mitarai, L.-O. Norlin, M. Palacz, J. Persson, H.A. Roth, R. Schubart, D. Seweryniak, T. Shizuma, O. Skeppstedt, D. Sohler, G. Sletten, W.B. Walters, M. Weiszflog, Z. Phys. A 356 (1996) 239.
[33] M. Górska, H. Grawe, D. Foltescu, D.B. Fossan, R. Grzywacz, J. Heese, K.H. Maier, M. Rejmund, H. Roth, R. Schubart, O. Skeppstedt, K. Spohr, Z. Phys. A 353 (1995) 233.
[34] F.P. Heßberger, S. Hofmann, D. Ackermann, V. Ninov, M. Leino, S. Saro, A. Andreyev, A. Lavrentev, A.G. Popeko, A.V. Yeremin, Eur. Phys. J. A 8 (2000) 521.
[35] D. Vermeulen, H.-G. Clerc, C.-C. Sahm, K.-H. Schmidt, J.G. Keller, G. Münzenberg, W. Reisdorf, Z. Phys. A 318 (1984) 157.
[36] A.G. Popeko, O.N. Malyshev, R.N. Sagaidak, A.V. Yeremin, Nucl. Instr. and Meth. B 126 (1997) 294.
[37] A.G. Popeko, O.N. Malyshev, A.V. Yeremin, S. Hofmann, Nucl. Instr. and Meth. A 427 (1999) 166.
[38] V.S. Nikolaev, I.S. Dmitriev, Phys. Lett. A 28 (1968) 277.
[39] F.P. Heßberger, G. Münzenberg, P. Armbruster, G. Berthes, W. Faust, S. Hofmann, W. Reisdorf, K.-H. Schmidt, H. Ewald, K. Gütter, in: Heavy Ion Interaction Around the Coulomb Barrier, Lecture Notes in Physics, vol. 317, Springer-Verlag, Berlin, 1988, p. 289.
[40] G. Vorobjev, D. Ackermann, D. Beck, K. Blaum, M. Block, A. Chaudhuri, Z. Di, S. Eliseev, R. Ferrer, D. Habs, F. Herfurth, F. Heßberger, S. Hofmann, H.-J. Kluge, P.G. Maero, A. Martín, G. Marx, M. Mazzocco, J.B. Neumayr, Y. Novikov, W. Plaß, C. Rauth, D. Rodríguez, C. Scheidenberger, L. Schweikhard, M. Sewtz, P. Thirolf, W. Quint, C. Weber Proc. Sci. (2006) (NIC-IX) 208.
[41] M. Block, D. Ackermann, K. Blaum, A. Chaudhuri, Z. Di, S. Eliseev, R. Ferrer, D. Habs, F. Herfurth, F.P. Heßberger, S. Hofmann, H.-J. Kluge, G. Maero, A. Martín, G. Marx, M. Mazzocco, M. Mukherjee, J.B. Neumayr, W.R. Plaß, W. Quint, S. Rahaman, C. Rauth, D. Rodríguez, C. Scheidenberger, L. Schweikhard, P.G. Thirolpf, G. Vorobjev, C. Weber, Hyperfine Interact. 173 (2007) 133.
[42] A. Martín, D. Ackermann, G. Audi, K. Blaum, M. Block, A. Chaudhuri, Z. Di, S. Eliseev, R. Ferrer, D. Habs, F. Herfurth, F.P. Heßberger, S. Hofmann, H.-J. Kluge, M. Mazzocco, M. Mukherjee, J.B. Neumayr, Yu. Novikov, W. Plaß, S. Rahaman, C. Rauth, D. Rodríguez, C. Scheidenberger, L. Schweikhard, P.G. Thirolf, G. Vorobjev, C. Weber, Eur. Phys. J.A 34 (2007) 341.
[43] S.A. Eliseev, M. Block, A. Chaudhuri, Z. Di, D. Habs, F. Herfurth, H.-J. Kluge, J.B. Neumayr, W.R. Plaß, C. Rauth, P.G. Thirolf, G. Vorobjev, Z. Wang, Nucl. Instr. and Meth. B 258 (2007) 479.
[44] C. Rauth, D. Ackermann, K. Blaum, M. Block, A. Chaudhuri, Z. Di, S. Eliseev, R. Ferrer, D. Habs, F. Herfurth, F.P. Heßberger, S. Hofmann, H.-J. Kluge, G. Maero, A. Martín, G. Marx, M. Mukherjee, J.B. Neumayr, W.R. Plaß, S. Rahaman, D. Rodríguez, C. Scheidenberger, L. Schweikhard, P.G. Thirolf, G. Vorobjev, C. Weber, Phys. Rev. Lett. 100 (2008) 012501.
[45] C. Rauth, D. Ackermann, G. Audi, M. Block, A. Chaudhuri, S. Eliseev, F. Herfurth, F.P. Heßberger, S. Hofmann, H.-J. Kluge, A. Martín, G. Marx, M. Mukherjee, J.B. Neumayr, W.R. Plaß, S. Rahaman, D. Rodríguez, L. Schweikhard, P.G. Thirolf, G. Vorobjev, C. Weber, Eur. Phys. J. Special Topics 150 (2007) 329.
[46] H.W. Gäggeler, D.T. Jost, A. Turler, P. Armbruster, W. Brüchle, H. Folger, F.P. Heßberger, S. Hofmann, G. Münzenberg, V. Ninov, W. Reisdorf, M. Schadel, K. Sümmerer, J.V. Kratz, U. Scherer, M.E. Leino, Nucl. Phys. A 502 (1989) 561c.
[47] M. Block, D. Ackermann, K. Blaum, A. Chaudhuri, Z. Di, S. Eliseev, R. Ferrer, D. Habs, F. Herfurth, F.P. Heßberger, S. Hofmann, H.-J. Kluge, G. Maero, A. Martín, G. Marx, M. Mazzocco, M. Mukherjee, J.B. Neumayr, W.R. Plaß, W. Quint, S. Rahaman, C. Rauth, D. Rodríguez, C. Scheidenberger, L. Schweikhard, P.G. Thirolf, G. Vorobjev, C. Weber, Eur. Phys. J. D 45 (2007) 39.
[48] C.N. Davids, B.B. Back, K. Bindra, D.J. Henderson, W. Kutschera, T. Lauritsen, Y. Nagame, P. Sugathan, A.V. Ramayya, W.B. Walters, Nucl. Instr. and Meth. B 70 (1992) 358.
[49] C.J. Gross, T.N. Ginter, D. Shapira, W.T. Milner, J.W. McConnell, A.N. James, J.W. Johnson, J. Mas, P.F. Mantica, R.L. Auble, J.J. Das, J.L. Blankenship, J.H. Hamilton, R.L. Robinson, Y.A. Akovali, C. Baktash, J.C. Batchelder, C.R. Bingham, M.J. Brinkman, H.K. Carter, R.A. Cunningham, T. Davinson, J.D. Fox, A. Galindo-Uribarri, R. Grzywacz, J.F. Liang, B.D. MacDonald, J. MacKenzie, S.D. Paul, A. Piechaczek, D.C. Radford, A.V. Ramayya, W. Reviol, D. Rudolph, K. Rykaczewski, K.S. Toth, W. Weintraub, C. Williams, P.J. Woods, C.-H. Yu, E.F. Zganjar, Nucl. Instr. and Meth. A 454 (2000) 12.
[50] M. Mazzocco F. Farinon, T. Glodariu, H. Geissel, A. Guglielmetti, N. Iwasa, M. La Commara, B. Martin, C. Mazzocchi, D. Pierroutsakou, M. Romoli, M. Sandoli, C. Signorini, F. Soramel, L. Stroe, E. Vardaci, H. Weick, M. Winkler, Nucl. Instr. and Meth. B, in: Proceedings of the EMIS-XV Conference, in press.
[51] F. Farinon, T. Glodariu, M. Mazzocco, A. Battistella, R. Bonetti, L. Costa, A. De Rosa, A. Guglielmetti, G. Inglima, M. La Commara, V.Z. Maidikov, B. Martin, C. Mazzocchi, D. Pierroutsakou, M. Romoli, M. Sandoli, C. Signorini, F. Soramel, L. Stroe, E. Vardaci, Nucl. Instr. and Meth. B, in: Proceedings of the EMIS-XV Conference, in press.